Aging Behavior of Al 6061 Alloy Processed by High-Pressure Torsion and Subsequent Aging

INTAN FADHLINA MOHAMED, SEUNGWON LEE, KAVEH EDALATI,
ZENJI HORITA, SHOICHI HIROSAWA, KENJI MATSUDA, and DAISUKE TERADA

A process to achieve strengthening in an Al 6061 alloy by grain refinement to ~200 nm using high-pressure torsion (HPT) and fine precipitation using aging treatment is studied. It is shown that although aging of the HPT-processed sample is effective for extra strengthening of the alloy, the imposed shear strain and the aging temperature should be selected carefully. The HPT processing after 5 turns leads high saturation hardness and tensile strength of 163 Hv and 470 MPa, respectively. The hardness at the saturation level remains the same during aging at 373 K (100 °C), while the hardness decreases by aging at 423 K (150 °C). When the disks are processed for 0.75 turns (lower shear strains) and aged at 373 K (100 °C), the hardness increases above the hardness level at the saturation because of the formation of B′ and β′ precipitates. Quantitative analyses indicate that three major hardening mechanisms contribute to the total hardening: grain boundary hardening through the Hall–Petch relationship, dislocation hardening through the Bailey–Hirsch relationship and precipitation hardening through the Orowan relationship. This study shows that the contribution of different strengthening mechanisms can be estimated using a linear additive relationship in ultrafine-grained aluminum alloys.

I. INTRODUCTION

THE Al 6000 alloy series, which are alloyed with Mg and Si, are known as typical age-hardenable alloys. A renewed study on precipitation hardening of Al-Mg-Si alloys has been led by industry especially in automotive applications in recent years. The most probable sequence of the precipitates during age hardening of the Al-Mg-Si alloys is supersaturate solid solution (SSSS) → clustering of Mg and Si atoms → GP-I zones → GP-II zones (β'' needle) → Mg_2Si (β' rods) → Mg_2Si (β plate).[1–7] In addition to this sequence, formation of some other intermediate phases of precipitates is reported depending on the excess contents of Si[8–12] or Mg.[13,14]

In addition to precipitation hardening, another strategy to improve the strength of Al alloys is grain refinement through the Hall–Petch relationship.[15,16] In order to achieve sig-

nificant grain refinement and produce bulk ultrafine-grained (UFG) materials, severe plastic deformation (SPD) techniques including high-pressure torsion (HPT), equal channel angular pressing (ECAP), and accumulative roll-bonding (ARB) are available.[17–30] Among the different SPD techniques, the HPT process is an attractive method which can be applied to control microstructures and phase transformations in various metallic materials,[23–25] hard-to-deform materials,[26–29] and even in ceramics[30] by introducing extremely large strains.

Since UFG alloys have a potential to exhibit high strength from multiple strengthening mechanisms including grain refinement, solid solution, dislocation entanglements, and precipitation,[20,31,32] it is essential to estimate the contribution of each of these factors to the total strengthening of the alloys. It was demonstrated that it is feasible to achieve a combined effect of grain refinement through the SPD process and fine precipitations through post-SPD aging in an Al-Ag alloy, where a combined effect was realized with a good strength and reasonable ductility.[33] Kim *et al.* reported a positive effect of aging on the strength of an ECAP-processed Al 6061 alloy.[34] They found that higher strength with a moderate level of ductility was achieved after combination of ECAP processing with post-ECAP aging.[34]

The contribution of different strengthening mechanisms to the total strength of UFG materials was investigated in different materials and rather contradicting conclusions were reported. Takaki *et al.*[35] proposed a strengthening model for UFG materials, in which the contribution of strength from dislocation accumulation should be ignored due to limitations in strain hardening. They suggested that the strengthening in UFG materials

INTAN FADHLINA MOHAMED, Ph.D. Student, SEUNGWON LEE, Technical Support Staff, KAVEH EDALATI, Research Fellow, and ZENJI HORITA, Professor, are with the Department of Materials Science and Engineering, Faculty of Engineering, Kyushu University, Fukuoka 819-0395, Japan, and also with the WPI, International Institute for Carbon-Neutral Energy Research (WPI-I2CNER), Kyushu University, Fukuoka 819-0395, Japan. Contact e-mail: intan@zaiko6.zaiko.kyushu-u.ac.jp SHOICHI HIROSAWA, Professor, is with the Department of Mechanical Engineering and Materials Science, Yokohama National University, Yokohama 240-8501, Japan. KENJI MATSUDA, Professor, is with the Graduate School of Science and Engineering for Research, University of Toyama, Toyama 930-8555, Japan. DAISUKE TERADA, Professor, is with the Department of Mechanical Science and Engineering, Faculty of Engineering, Chiba Institute of Technology, Narashino 275-0016, Japan.
Manuscript submitted October 20, 2014.
Article published online March 18, 2015.

is mainly due to grain boundary strengthening. In accordance with the Takaki's report, Edalati et al.[36,37] also suggested that the grain boundary strengthening is the main strengthening mechanism in UFG pure metals and single-phase alloys. Gubicza et al.,[38] Starink et al.,[24] and Joni et al.[27] reached a different conclusion and suggested that the strengthening by dislocation accumulation has the most significant impact on the strength of UFG materials. Several other studies, however, reported that the different strengthening mechanisms contribute to the total strengthening through a linear superposition relationship.[39–41] It is of particular scientific and engineering importance to find how the different strengthening mechanisms contribute to the hardening of UFG Al-based alloys.

In this work, HPT is adopted for grain refinement in an age-hardable Al 6061 alloy. Simultaneous strengthening both by grain refinement and dislocation accumulation as well as by fine precipitation through subsequent aging is investigated, and the contribution of various strengthening mechanisms to the total strength is evaluated quantitatively.

II. EXPERIMENTAL MATERIALS AND PROCEDURES

The material used in this study is a commercial Al 6061 alloy which contains 0.96 pct Mg, 0.59 pct Si, 0.29 pct Cu, 0.29 pct Fe, 0.02 pct Cr, 0.01 pct Zn, and 0.01 pct Ti with balance of Al in wt pct. The material was received in a form of a cold-rolled sheet with 1 mm thickness. Disks of 1 mm thickness and 10-mm diameter were then cut from the sheet by a wire-cutting electric discharge machine (EDM). They were solution treated at 803 K (530 °C) for 4 hours in an air atmosphere and then immediately quenched into ice water.

Each disk with 1 mm thickness was processed by HPT at room temperature (RT) under an applied pressure of 6 GPa for 0.75, 1, and 5 turns at a rotation speed of 1 rpm. The thickness of the disks was reduced to 0.79 to 0.8 mm during the HPT processing and this thickness was used for calculation of the equivalent strain. Zero slippage between the anvils and the disk was confirmed according to the measurement as described earlier.[42] The HPT-processed disks were aged at 373 K or 423 K (100 °C or 150 °C) in air for certain periods of time.

Vickers microhardness was measured by application of 50 g for a dwell time of 15 seconds. The measurements were made at equal distances from the disk center to the edge along 8 different radial directions as illustrated in Figure 1.

The HPT-processed samples through $N = 0.75$ before and after the aging treatment were polished to a thickness of ~0.50 mm and tensile specimens were cut from the polished disks using EDM as in Figure 1 with gage lengths, widths, and thicknesses of 1.5, 0.7, and 0.5 mm, respectively. Tensile tests were carried out at room temperature with an initial strain rate of 2×10^{-3} s^{-1}.

The HPT-processed disks before and after the aging treatment were grounded to a thickness of 0.4 mm, punched to small disks with 3 mm-diameters as shown
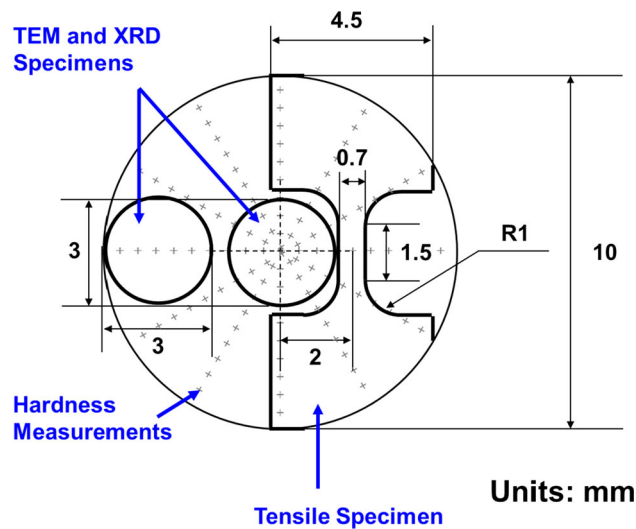

Fig. 1—Schematic illustration of HPT disk and locations for hardness measurements, tensile specimen, and TEM and XRD disks.

in Figure 1. They were further ground to a thickness of 0.12 mm and were thinned for perforation by a twin-jet electro-polisher using a solution of 30 pct HNO$_3$ and 70 pct CH$_3$OH at a temperature of 260 K (-13 °C) with an applied voltage of 10 V. The microstructural observations were performed in a conventional transmission mode with parallel beam using a Hitachi H-8100 transmission electron microscope (TEM) at an accelerating voltage of 200 kV. Selected area electron diffraction (SAED) patterns were taken around regions having diameter of 6.3 μm. This diameter, which was measured by inserting the selected area aperture and taking an image, was selected to cover appreciable numbers of grains. Scanning transmission electron microscopy (STEM) images were recorded, and elemental mapping was performed using energy-dispersive X-ray spectroscopy (EDS) with a JEM-3200FSK microscope at an accelerating voltage of 300 kV.

The 3 mm disks prepared for the TEM samples were also used for X-ray diffraction (XRD) analysis using the Cu Kα radiation with an accelerating voltage of 40 kV and a current of 40 mA. The dislocation densities were measured by employing the linear Williamson–Hall relationship[43] while excluding influence of the Kα_2 radiation.

III. RESULTS

A. Mechanical Properties

Figure 2(a) shows a plot of Vickers microhardness against the distance from the disk center for 0.75, 1, and 5 turns under a pressure of 6 GPa. The hardness increases with increasing the distance and saturates to a constant level when approaching the edge of the disk. The plots also show that the hardness increases with increasing the number of turns, especially at shorter distances from the disk center.

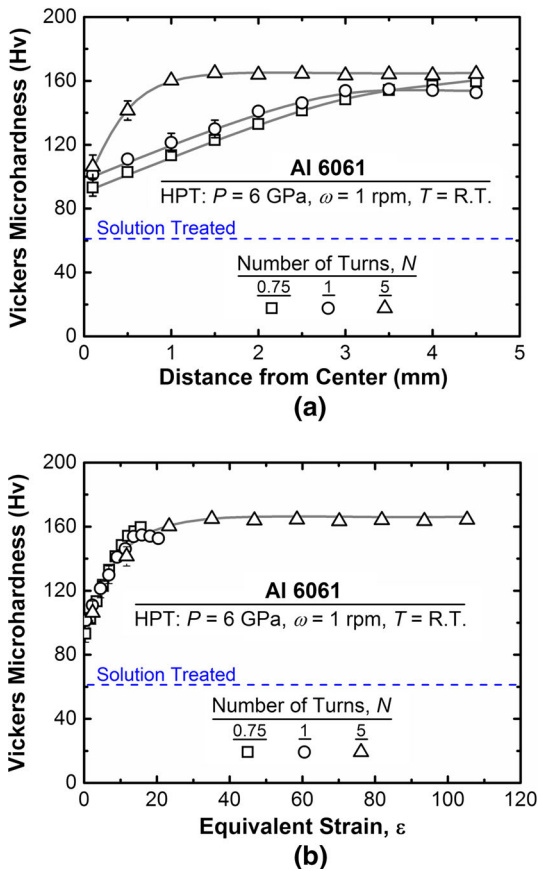In Figure 2(b), all hardness values in Figure 2(a) are re-plotted as a function of equivalent strain. Here, the

Fig. 2—Vickers microhardness plotted against (*a*) distance from disk center and (*b*) equivalent strain for samples processed by HPT through 0.75, 1, and 5 turns.

equivalent strain imposed on each disk is calculated by the following equation[44]:

$$\varepsilon = (1 - s) \int_0^N \frac{2\pi r}{\sqrt{3} t(N)} dN \qquad [1]$$

where *r* is the distance from the disk center, *N* is the number of turns, *s* is the fraction of slippage, and $t(N)$ is the disk thickness after HPT processing for *N* turns. Since the thickness reached a constant value of 0.79 to 0.8 mm after any turns and no slippage occurred between the sample and the anvils, Eq. [1] may be simplified in the following form[45]:

$$\varepsilon = \frac{2\pi r N}{\sqrt{3} t} \qquad [2]$$

Now, all hardness values fall well on a single monotonic line represented by a unique function of the equivalent strain in Figure 2(b). The hardness increases with straining, levels off at an equivalent strain of ~20 and saturates to 163 Hv with further straining. A similar behavior of the hardness with respect to straining was reported in many pure metals and alloys.[26,30, 44–54] The steady-state hardness after HPT processing in Figure 2(b) is almost 170 pct higher than that in the Al 6061 alloy processed by solution treatment, and this hardness increase is twice as high as the hardness
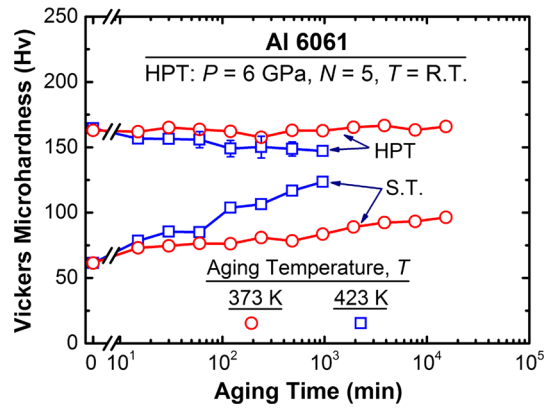

Fig. 3—Variation of hardness with aging time for samples processed by solution treatment and HPT through 5 turns.

increase after processing by ECAP for four passes.[32] It should be noted that the steady state at large strains is reached by a balance between the hardening due to lattice defects generation and the softening due to lattice defects and dislocations annihilation through dynamic recovery and dynamic recrystallization.[24,46,50]

To examine the aging behavior, the samples after HPT processing for *N* = 5 were aged at temperatures of 373 K (100 °C) and 473 K (200 °C) for total periods up to 14 days as in Figure 3. It should be noted that this examination was carried out at the saturation region where the steady state was established with straining. The results show that the hardness decreases from the beginning when the sample is aged at 423 K (150 °C). When aged at 375 K (102 °C), there are no appreciable changes in the hardness even after prolonged aging for 10 days.

The material processed up to saturation level is softened from an initial stage of aging and this is considered to be not only due to dislocation recovery and grain growth but also due to coarsening of precipitates with a stable form. Based on earlier reports,[34,55–57] it is envisaged that metastable phases which are essential for strengthening in age-hardenable Al alloys are evolved quickly when the alloy is severely deformed before aging because of abundance of lattice defects and fast atomic diffusion. Moreover, heterogeneous nucleation and coarsening of stable precipitates become predominant in SPD-processed alloys, which result in suppression of transgranular precipitation of fine metastable particles. Because the precipitation process is competitive among the nucleation sites in grain boundaries, dislocations, and the matrix, optimization should be important in selecting imposed strain and aging temperature in order to achieve simultaneous strengthening by grain refinement and fine precipitation.

Thus, aging was further carried out at a reduced temperature of 375 K (102 °C) using samples processed for lower numbers of turns as *N* = 0.75 with reduced equivalent strain. Figure 4(a) shows that the aging behavior after HPT processing for *N* = 0.75 at five different positions with equivalent strains of ε = 0.3, 3.5, 6.9, 10.4, and 13.9. At the positions with higher equivalent strains of ε = 10.4 and 13.9, the hardness increases above the value of the as-HPT-processed state
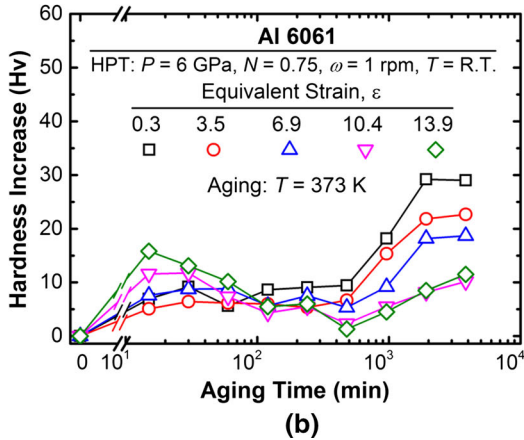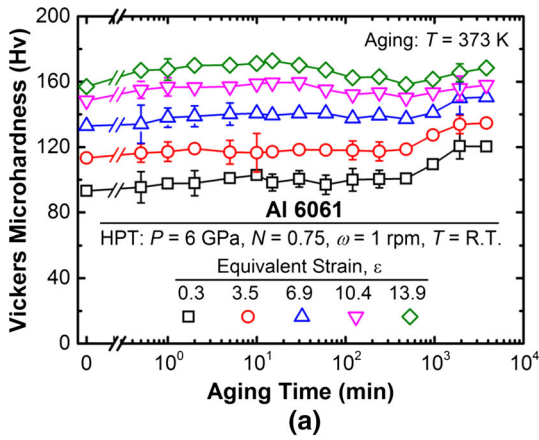
(a)

(b)

Fig. 4—Variation of (a) hardness and (b) hardness increase with aging time for sample processed by HPT through 0.75 turns.
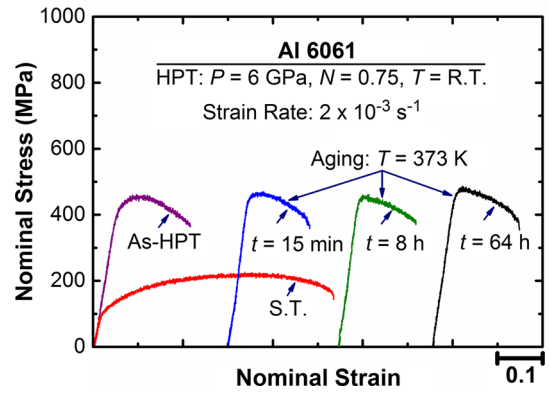

Fig. 5—Nominal stress vs nominal strain curves for samples processed by HPT for 0.75 turns and subsequently aged at 353 K (80 °C) for 15 min, 8, and 64 h including solution-treated sample.

from the beginning of aging and reaches a peak after 15 minutes to the hardness level of ~175 Hv. This value is appreciably higher than the hardness level of 163 Hv at the steady state. Thereafter, the hardness decreases with aging and increases again after 8 hours of aging. At lower equivalent strains as $\varepsilon = 0.3$ and 3.5, the hardness after the HPT processing is low but increases gradually from the beginning of the aging. Meanwhile, at the intermediate range of equivalent strain ($\varepsilon = 6.4$), the hardness behavior exhibits a trend between those of $\varepsilon = 0.3$ and 13.9.

The increase in hardness with aging at various equivalent strains is more clearly demonstrated in Figure 4(b). The hardness at $\varepsilon = 10.4$ and 13.9 reaches the peak earlier, while the hardness at $\varepsilon = 0.3$ and 3.4 shows no clear peak. Kim et al.[34] also reported a similar aging behavior in an Al 6061 alloy after processing by ECAP. This behavior can be attributed to an increase in dislocation density and rapid diffusion at higher equivalent strain which lead to the rapid formation of precipitates.[57,58]

Figure 5 shows the stress–strain curves after tensile testing of the samples processed by HPT for $N = 0.75$ and subsequent aging at 373 K (100 °C). The tensile testing was carried out at room temperature with an initial strain rate of 2×10^{-3} s^{-1}. The strength significantly increases by the HPT processing (460 MPa)

and becomes almost twice as high as the solution-treated state (225 MPa) with an elongation to failure retained to a reasonable extent of 17 pct. The tensile strength increases to 470 MPa at the peak aging for 15 minutes and decreases to 460 MPa after 8 hours of aging. However, the tensile strength increases to a higher value as 485 MPa when the aging is prolonged to 64 hours. It should be noted that the trend of the tensile strength (Figure 5) and the increasing in hardness (Figure 4(b)) during the aging are consistent to each other.

B. Microstructure Evolution

Figures 6(a) through (c) show TEM microstructures of the samples after HPT processing at room temperature. They correspond to microstructural evolutions at the initial, intermediate, and steady-state stages of straining, respectively. For the initial straining of $\varepsilon = ~1$ ($N = 0.75$, $r = 0.3$ mm) in Figure 6(a), the bright-field and dark-field TEM images show microstructures with rather low dislocation density within the grains. The SAED pattern displays less spots in Figure 6(a) when compared to those in Figures 6(b) and (c). Since the diameters of selected area were the same (6.3 μm) in three SAED patterns, the presence of less spots in the SAED pattern of Figure 6(a) demonstrates the presence of larger grains at low strains. The presence of larger grains in Figure 6(a) is apparent from the dark-field images as well. It should be noted that the dark-field images were taken with the diffracted beams indicated by arrows in the SAED patterns.

When the equivalent strain is increased to $\varepsilon = ~16$ ($N = 1$, $r = 3.5$ mm), the grain size is refined to an average size of ~310 nm as in Figure 6(b). With further straining to $\varepsilon = ~80$ ($N = 5$, $r = 3.5$ mm), the grain size reaches a steady-state level of ~200 nm as in Figure 6(c). The appearance of extra diffracted beams which are distributed in a ring form in the SAED pattern suggests that the microstructural change is dominated by conversion of low-angle to high-angle boundaries at large strains.

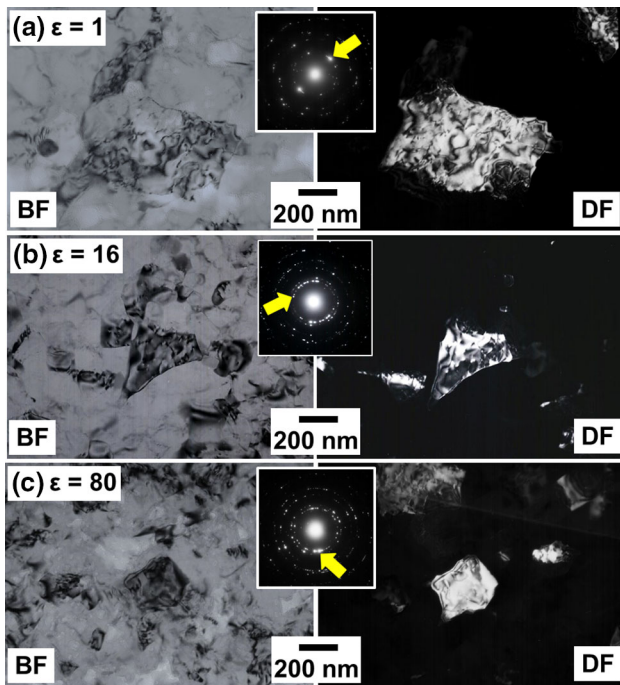Figure 7 shows bright-field and dark-field images including SAED patterns after the HPT processing for

Fig. 6—TEM bright-field images (left), dark-field images (right), and corresponding SAED patterns for samples processed by HPT for (a) $\varepsilon = 1$ ($N = 0.75$, $r = 0.3$ mm), (b) $\varepsilon = 16$ ($N = 1$, $r = 3.5$ mm), and (c) $\varepsilon = 80$ ($N = 5$, $r = 3.5$ mm). Dark-field images were taken with diffracted beams indicated by arrows in SAED patterns.
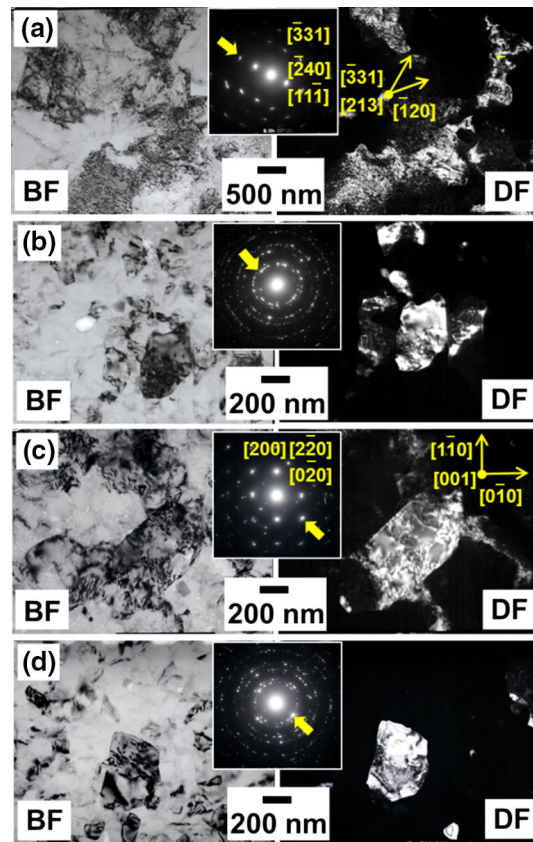

Fig. 7—TEM bright-field images (left), dark-field images (right), and corresponding SAED patterns for samples processed by HPT for (a, c) $\varepsilon = 1$ ($N = 0.75$, $r = 0.3$ mm) and (b, d) $\varepsilon = 12$ ($N = 0.75$, $r = 3.5$ mm) and subsequently aged at 373 K (100 °C) for (a, b) 15 min and (c, d) 64 h. Dark-field images were taken with diffracted beams indicated by arrows in SAED patterns.

$N = 0.75$ and subsequent aging at 373 K (100 °C) for (a, b) 15 minutes and (c, d) 64 hours, where (a) and (c) were taken from the center of disk ($r = 0.3$ mm, $\varepsilon = \sim1$) and (b) and (d) were taken from the edge of disks ($r = 3.5$ mm, $\varepsilon = \sim12$). When compared with the microstructures after HPT processing as shown in Figures 6(a) and (b), there appear to be no appreciable changes in the grain size after 15 minutes of aging. No appreciable grain growth occurs even after prolonged aging for 64 hours. The grain size distribution, as shown in Figure 8, indicates that the grain sizes remain reasonably the same after the aging process.

Detailed inter-atomic d-spacing analysis on the SAED pattern, as shown in Figure 9 for a sample processed through $\varepsilon = \sim12$ and aged for 64 hours at 373 K (100 °C), reveals that two kinds of precipitates form after aging: hexagonal Mg_2Si precipitates (β') and $Mg_9Al_3Si_7$ precipitates (B'). EDS mapping, as shown in Figure 10, also suggests that there are many Mg-rich and Si-rich precipitates which can be Mg_2Si and $Mg_9Al_3Si_7$ precipitates. Besides such common particles, the EDS mapping also reveals that there are particles rich in Si, Fe, Cr, and Mn as marked by an yellow arrow in Figure 10. EDS mapping after solution treatment, as shown in Figure 11, confirmed that such particles were also present in the solution-treated sample as well as in the HPT-processed sample and they were not formed during the aging process. The fraction of these particles, however, significantly decreases after the HPT process-ing due to their dissolution in the matrix (see EDS mapping after HPT in Figure 12).

C. Dislocation Density

Dislocation density can be calculated from the XRD peak broadening using the Williamson–Hall method[43]

$$\frac{\beta \cos \theta}{\lambda} = \frac{0.9}{D} + \frac{2\varepsilon \sin \theta}{\lambda} \qquad [3]$$

$$\rho = 14.4 \frac{\varepsilon^2}{b^2} \qquad [4]$$

where β is the full width at half maximum in rad, λ is the wavelength of X-ray beam (0.1542 nm for Cu Kα), D is the crystallite size, ε is the lattice strain, θ is the Bragg angle, ρ is the dislocation density, and b is the Burgers vector (0.286 nm for Al). The values of ρ are plotted against the aging time in Figure 13 for several samples processed by HPT processing for different levels of strain. There are more dislocations in the early stage of straining ($\varepsilon = \sim1$), but less dislocations with further straining to $\varepsilon = \sim12$. During aging at 373 K (100 °C), the dislocation density decreases significantly but the reduction is more intense at $\varepsilon = \sim12$ than $\varepsilon = \sim1$. The relatively low dislocation density at the large strain is established as a result of dislocation absorption at high-angle grain boundaries.[51,59] Moreover, this can be
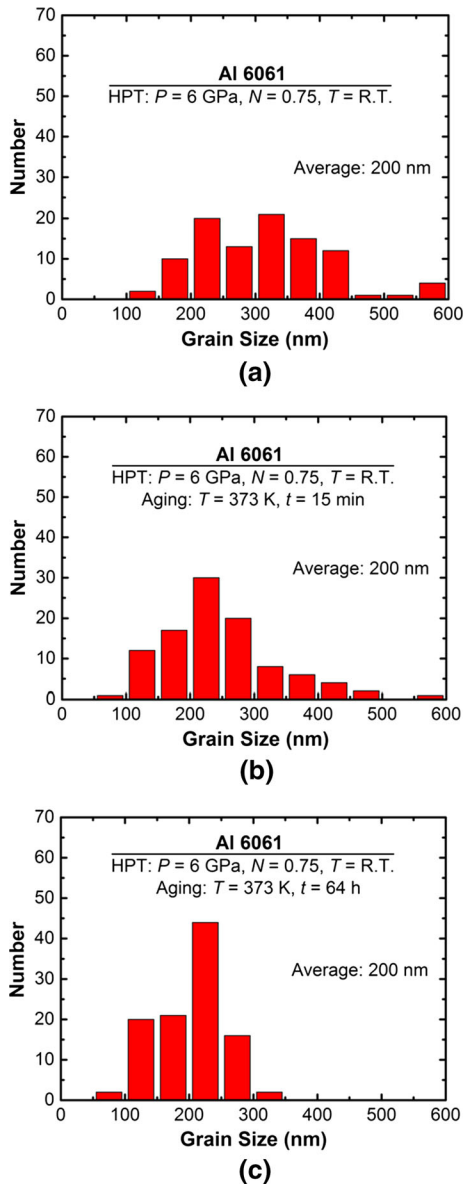
Fig. 8—Grain size distribution for sample processed by HPT for 0.75 turns and subsequently aged at 373 K (100 °C) for (a) 0, (b) 15 min, and (c) 64 h.
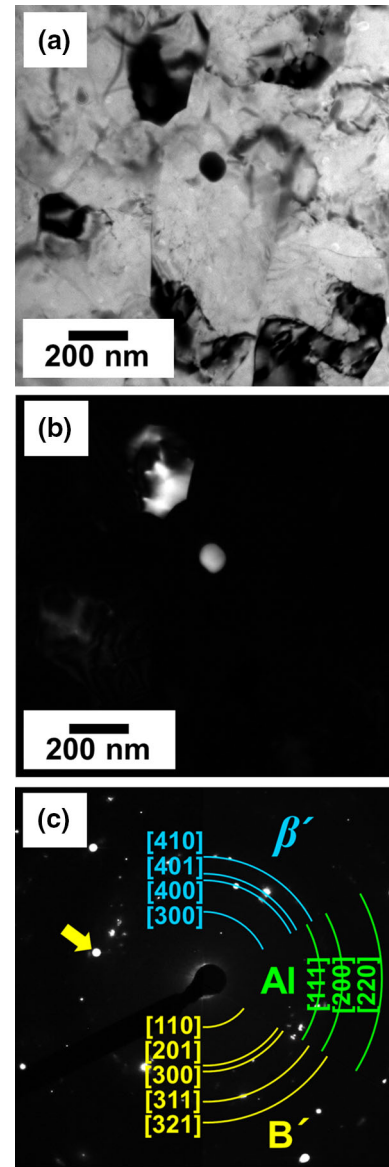

Fig. 9—TEM (a) bright-field image, (b) dark-field image, and (c) corresponding SAED patterns for sample processed by HPT for 0.75 turns and subsequently aged at 373 K (100 °C) for 64 h. Dark-field image was taken with diffracted beam indicated by arrow in SAED pattern.

explained by an increase in the stored energy which is proportional to imposed strain. An increase in the stored energy leads to an increase in driving force for atomic diffusion and hence for enhanced recovery process to expedite dislocation annihilation.

IV. DISCUSSION

The high strength of this age-hardenable Al 6061 alloy may be attributed to (1) solid solution strengthening, (2) grain refinement strengthening, (3) dislocation strengthening, and (4) precipitation strengthening. As demonstrated in this study, with reduced deformation ($N = 0.75$) and reduced aging temperature [$T = 373$ K (100 °C)], it is possible to realize further strengthening the ultrafine-grained Al 6061 alloy by aging. This indicates that it is possible to achieve simultaneous strengthening due to grain refinement and fine precipitation through HPT processing and subsequent aging. Table I gives contributions from not only grain refinement (ΔHV_{GB}) and fine precipitation (ΔHV_P) but also dislocations (ΔHV_{Dis}) and solid solution (ΔHV_{SS}) for the Al 6061 alloy as well as for two other Al alloys (Al 2024 and Al-4 pctCu). It should be noted that the data for the Al 2024 and Al-4 pctCu alloys were taken from other works of the authors.[60,61] In Table I, HV_0 represents the hardness of coarse-grained annealed Al with a purity level of 99.999 pct[62] and HV_{Total} represents the sum of four different strengthening mechanisms which is calculated by[63]
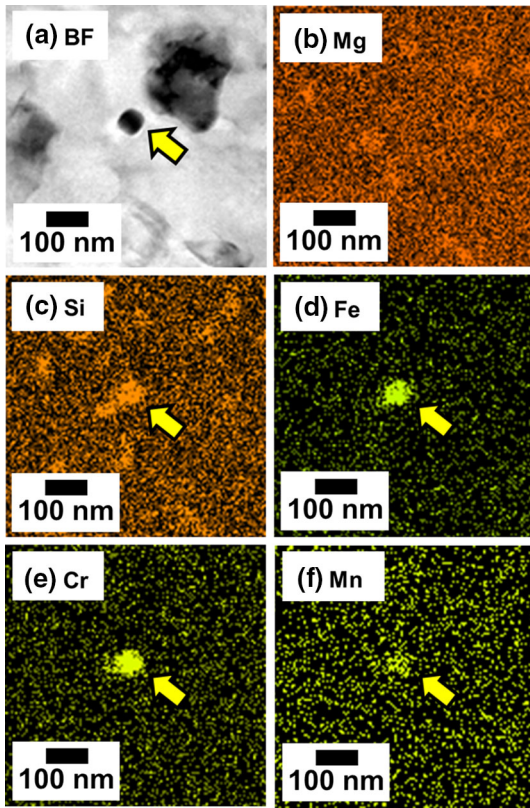
Fig. 10—(a) STEM bright-field image and corresponding EDS mappings with (a) Al, (b) Mg, (c) Si, (d) Fe, (e) Cr, and (f) Mn for sample processed by HPT for 0.75 turns and subsequently aged at 373 K (100 °C) for 64 h.

$$\Delta HV_{Total} = HV_0 + \Delta HV_{SS}$$
$$+ (\Delta HV_{GB}^n + \Delta HV_{Dis}^n + \Delta HV_P^n)^{1/n} \quad [5]$$

where n has a value between 1 and 2. Table I indicates that HV_{Total} calculated using $n = 1$ (linear superposition) is reasonably consistent with the experimental measurements ($HV_{Measured}$), but HV_{Total} calculated using $n = 2$ (pythagorean superposition) is lower than the experimental levels. More details on calculations are discussed below.

In general, the solid solution strengthening may be estimated by the Fleischer equation[64] or by the Labusch equation[65]

$$\Delta\tau_{SS} = \frac{G|\varepsilon_G' - m\varepsilon_b|^{3/2} c^{1/2}}{\alpha} \quad [6]$$

$$\Delta\tau_{SS} = \frac{G[\varepsilon_G'^2 + (15\varepsilon_b)^2]^{2/3} c^{2/3}}{\phi} \quad [7]$$

where $\Delta\tau_{SS}$ is the increase in shear stress due to solution hardening which can be converted to normal stress or hardness using the well-known relationships of $\Delta\sigma = 3\Delta\tau$ and $\Delta HV \approx 3\Delta\sigma$, G is the shear modulus, ε_G' is the modulus mismatch parameter, m is the mean
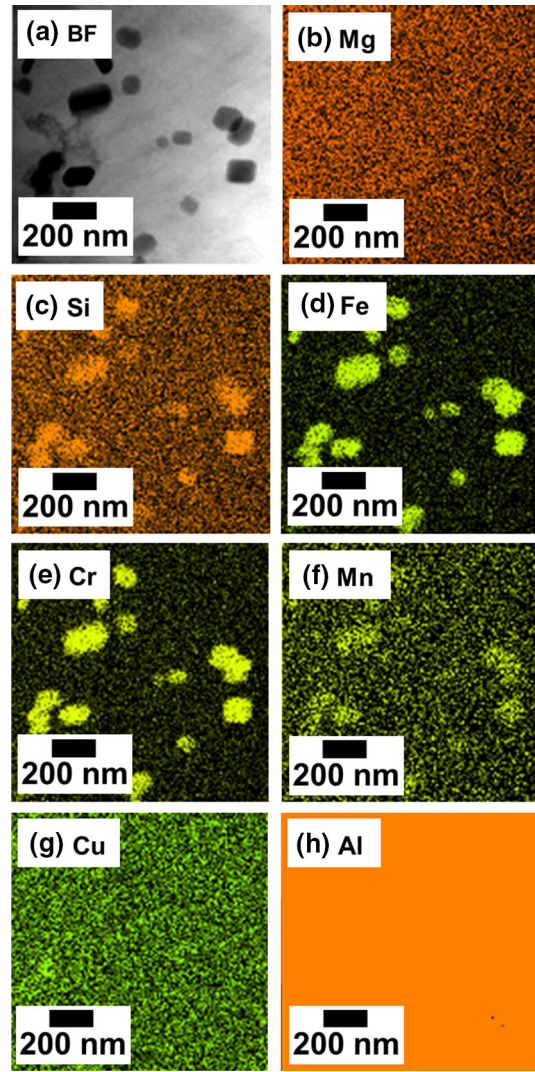

Fig. 11—(a) STEM bright-field image and corresponding EDS mappings with (a) Al, (b) Mg, (c) Si, (d) Fe, (e) Cr, and (f) Mn for solution-treated sample.

orientation factor for fcc polycrystalline matrix, ε_b is the atomic size mismatch, c is the solute atom concentration, and α and ϕ are two constants. For the present Al 6061 alloy, the estimation has used as $G = 26$ GPa, $m = 3$, $\alpha = 700$, and $\phi = 550$. Furthermore, for a major alloying element of Mg, $c = 0.011$, $\varepsilon_G' = 0.71$, and $\varepsilon_b = 0.10$ and for the second major alloying element Si, $c = 0.0056$, $\varepsilon_G' = -0.21$, and $\varepsilon_b = -0.04$.[66] Since c is as low as 0.0014, 0.0010, 0.0012, <0.0001, <0.0001 for Fe, Cr and Cu, Ti and Zn, respectively, the effect of these elements on solution hardening was neglected. Thus, it follows that ΔH_{SS} for solution hardening by Mg is 1 and 5 Hv using the Fleischer and Labusch equations, respectively. ΔH_{SS} for solution hardening by Si is as small as 0.07 and 0.7 Hv using the Fleischer and Labusch equations, respectively, and can be reasonably neglected. The contribution of solution hardening to the total hardening appears to be small in this 6061 alloy in consistency with an earlier report on HPT processing of several alloys.[37]
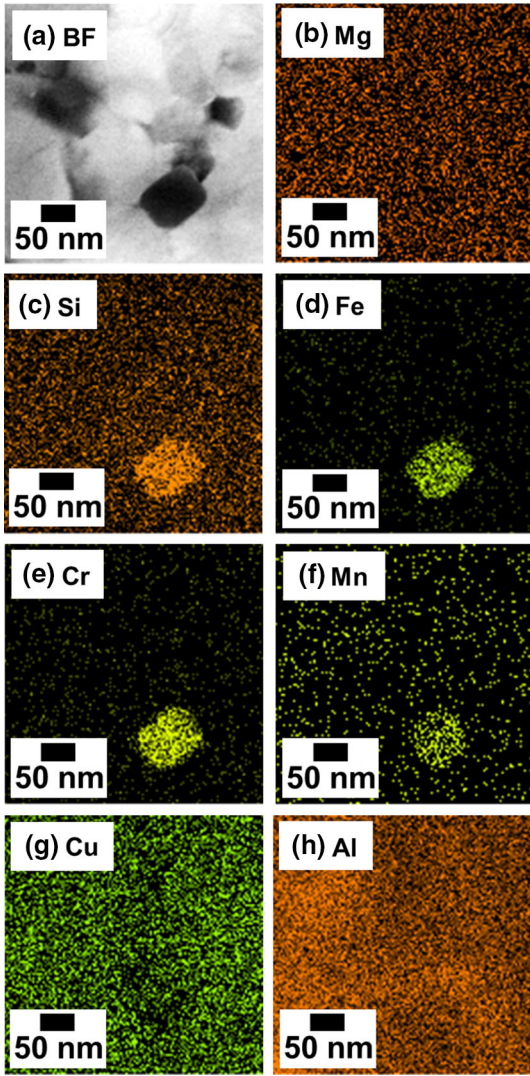
Fig. 12—(*a*) STEM bright-field image and corresponding EDS mappings with (a) Al, (b) Mg, (c) Si, (d) Fe, (e) Cr, and (f) Mn for sample processed by HPT for 0.75 turns.
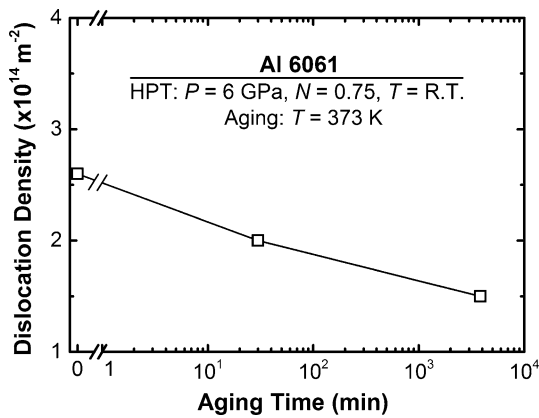

Fig. 13—Variation of dislocation density with aging time for samples processed by HPT at $\varepsilon = 12$ and subsequently aged at 373 K (100 °C).

The grain refinement strengthening, $\Delta\sigma_{GB}$, is described by the Hall–Petch equation[15,16]:

$$\Delta\sigma_{GB} = \sigma_y - \sigma_0 = \frac{k_y}{\sqrt{d}} \qquad [8]$$

where σ_y is the Hall–Petch strength, d is the average grain size, σ_0 is the friction stress, and k_y is the Hall–Petch slope (0.166 MNm$^{-3/2}$[20]). The grain refinement to ~310 nm by HPT processing at $N = 0.75$ leads to strengthening by 91 Hv. This contribution remains unchanged since the ultrafine grains are retained with the same size even after prolonged aging for 64 hours.

Meanwhile, the XRD analyses detected a high dislocation density in the alloy after HPT processing. Dislocation tangles and networks within the grains and near grain boundaries make dislocation glide more difficult and hence increase the strength. It is then derived that the dislocation strengthening comes to the strength enhancement by ~22 Hv after HPT processing for $N = 0.75$. However, this hardening is followed by softening with aging, as shown in Figure 12, due to annihilation of dislocation. It should be noted that the strengthening by dislocations, $\Delta\tau_{Dis}$, is calculated as[67]

$$\Delta\tau_{Dis} = \alpha' G b \sqrt{\rho} \qquad [9]$$

where $\alpha' = 0.2$ for fcc metals.

The precipitation strengthening results from the precipitate's ability to obstruct dislocation movement. For small and coherent precipitates, a dislocation cutting mechanism is dominant.[68]

$$\Delta\tau_C = \frac{\pi \gamma r_P}{\lambda' b} \qquad [10]$$

where $\Delta\tau_C$ is the stress needed to cut a dislocation, γ is the surface energy (0.98 J/m^2 for Al[69]), r_P is the radius of particles, and λ' is the inter-particle spacing given by $\lambda' = L - d_P$ (L is the distance between particles and d_p is the particle diameter). Estimation of the strengthening may be given by the following Orowan equation through the bowing mechanism, when the particle sizes are higher than a critical value:[70]

$$\Delta\tau_P = \frac{Gb}{\lambda'} \qquad [11]$$

where $\Delta\tau_P$ is the Orowan stress. The critical radius, r_C, for transition from the cutting mechanism to the Orowan mechanisms is given by the following equations.[68]

$$r_C = \frac{2Gb^2}{\pi \gamma} \qquad [12]$$

$$r_C = 20b \qquad [13]$$

Estimations using Eqs. [12] and [13] yield to $r_C = 14$ and 6 nm, respectively. Since the average particle size in this study is 30 nm ($r_P = 15$ nm), the dominant mechanism for precipitate hardening should be bowing through the Orowan relationship. The method of estimating the contribution from the particle strengthening is adopted from a previous report.[71] Assuming that there are 3

Table I. Estimated Contribution of Different Hardening Mechanisms in Comparison with Experimental Measurements for Al-4 wt pct Cu, Al 2024, and Al 6061 Samples Processed by HPT After 0.75 Turns and Subsequently Aged (All Values are in Hv)

Aging	Al-4wt pct Cu (N = 5)				Al 2024 (N = 5)		Al 6061 (N = 0.75)	
	0	353 K (80 °C) 5 min	353 K (80 °C) 20 min	353 K (80 °C) 120 h	0	423 K (150 °C) 4 h	0	373 K (100 °C) 64 h
HV_0	20	20	20	20	20	20	20	20
ΔHV_{SS}	4.2–7	4.2–7	4.2–7	4.2–7	4.5–12.8	4.5–12.8	1–5	1–5
ΔHV_{GB}	86	86	78	64	81	78	91	91
ΔHV_{Dis}	16	14	14	13	41	33	22	17
ΔHV_P	unknown	unknown	52	51	unknown	68	unknown	49
HV_{Total} ($n = 1$)	>131	>129	171	155	>154	211	>138	182
HV_{Total} ($n = 2$)	>115	>114	121	109	>124	141	>119	129
$HV_{Measured}$	205	214	190	146	253	261	157	169
Reference	[61]				[60]		This work	

HV_0 hardness of coarse-grained pure Al, ΔHV_{SS} solution hardening, ΔHV_{GB} grain boundary hardening, ΔHV_{Dis} dislocation hardening, ΔH_P precipitation hardening, HV_{Total} total hardening calculated by Eq. [5], $HV_{Measured}$ measured Vickers hardness.

particles within a grain, as shown in Figure 9, and they are equally distributed, the average distance between two neighboring particles including the distance from one particle to the adjacent grain boundary is $\lambda' = 138$ nm based on the observation that the particle size is ~30 nm and the grain size is ~200 nm. From Eq. [4], the calculation gives rise to $\Delta\tau_P = 54$ MPa or a hardness increase of $\Delta HV_P = 49$ Hv.

Therefore, the cooperative interaction of precipitates, grain boundaries, and dislocations results in the appreciable strengthening of ultrafine grain Al 6061 alloy. It should be noted that the hardness increase due to precipitation (30 Hv) is smaller than the calculated value of hardness (49 Hv). Hence, it is suggested that this smaller value is due to the presence of some grains that are free of precipitates. If only ~60 pct of the total grains contain 3 precipitates, it is adequate to reach measured value of 30 Hv in this study. It is consistent with overall microstructure observation that the distributions of particles are not homogeneous among all grains because of preferable nucleation of precipitation at dislocations and grain boundaries.

V. CONCLUSIONS

1. The Vickers microhardness data for an Al 6061 alloy after High-pressure torsion (HPT) processing for 0.75, 1, and 5 turns lie well on a single curve when they are plotted against equivalent strain. The hardness increases with straining and saturates to a constant level of 163 HV at large strains.
2. TEM observation reveals that the grain size is refined to ~200 nm at the saturation.
3. The saturation hardness remains almost unchanged during aging at 373 K (100 °C) but gradually decreases by aging at 423 K (150 °C), suggesting that the aging temperature of 423 K (150 °C) is too high to achieve extra hardening through precipitation of fine particles.

4. Simultaneous strengthening by fine precipitation and grain refinement occurs when the sample processed at relatively low strains is aged at low temperatures as 373 K (100 °C).
5. The tensile test shows that the strength significantly increases to more than 400 MPa with some ductility reserved after HPT or after post-HPT aging.
6. Three hardening mechanisms as grain refinement hardening, dislocation hardening, and precipitation hardening contribute significantly to the total hardening, while the effect of solution hardening is small.
7. The contribution of different hardening mechanisms to the total hardness can be estimated using a linear additive relationship in ultrafine-grained aluminum alloys.

REFERENCES

1. I. Dutta and S.M. Allen: *J. Mater. Sci. Lett.*, 1991, vol. 10, pp. 323–26.
2. A. Lutts: *Acta Metall.*, 1961, vol. 9, pp. 577–86.
3. C. Panseri and T. Faderighi: *J. Inst. Met.*, 1966, vol. 94, pp. 99–107.

4. G. Thomas: *J. Inst. Met.*, 1961, vol. 90, pp. 57–63.
5. M.H. Jacobs: *Philos. Mag.*, 1972, vol. 26, pp. 1–13.
6. C.D. Marioara, H. Nordmark, S.J. Anderson, and R. Holmestad: *J. Mater. Sci.*, 2006, vol. 41, pp. 471–78.
7. C. Ravi and C. Wolverton: *Acta Mater.*, 2004, vol. 52, pp. 4213–27.
8. K. Matsuda, S. Ikeno, T. Sato, and A. Kamio: *Scripta Mater.*, 1995, vol. 32, pp. 1175–80.
9. K. Matsuda, S. Ikeno, T. Sato, and A. Kamio: *Scripta Mater.*, 1996, vol. 34, pp. 1797–1802.
10. K. Matsuda, T. Naoi, K. Fujii, Y. Uetani, T. Sato, A. Kamio, and S. Ikeno: *Mater. Sci. Eng. A*, 1999, vol. 262, pp. 232–37.
11. K. Matsuda, Y. Sakaguchi, Y. Miyata, Y. Uetani, T. Sato, A. Kamio, and S. Ikeno: *J. Mater. Sci.*, 2000, vol. 35, pp. 179–89.
12. S.J. Andersen, C.D. Marioara, A. Froseth, R. Vissers, and H.W. Zandbergen: *Mater. Sci. Eng. A*, 2005, vol. 390, pp. 127–38.
13. M. Kanno, H. Suzuki, and Y. Shiraishi: *J. Jpn Inst. Metals*, 1979, vol. 43, pp. 81–86.
14. Y. Ohmori, L.C. Doan, Y. Matsuura, S. Kobayashi, and K. Nakai: *Mater. Trans.*, 2001, vol. 42, pp. 2576–83.
15. E.O. Hall: *Proc. Phys. Soc. B*, 1951, vol. 64, p. 747.
16. N.J. Petch: *J. Iron Steel Inst.*, 1953, vol. 174, p. 25.
17. R.Z. Valiev, Y. Estrin, Z. Horita, T.G. Langdon, M.J. Zehetbauer, and Y.T. Zhu: *JOM*, 2006, vol. 58 (4), pp. 33–39.
18. R.Z. Valiev, R.K. Islamgaliev, and I.V. Alexandrov: *Prog. Mater Sci.*, 2000, vol. 45, pp. 103–89.
19. R.Z. Valiev and T.G. Langdon: *Prog. Mater Sci.*, 2006, vol. 51, pp. 881–981.
20. G. Nurislamova, X. Sauvage, M. Murashkin, R.K. Islamgaliev, and R.Z. Valiev: *Philos. Mag. Lett.*, 2008, vol. 88, pp. 459–66.
21. N. Kamikawa, X. Huang, N. Tsuji, and N. Hansen: *Acta Mater.*, 2009, vol. 57, pp. 4198–4208.
22. Z. Horita, T. Fujunami, M. Nemoto, and T.G. Langdon: *J. Mat. Proc. Tech.*, 2001, vol. 117, pp. 288–92.
23. A.P. Zhilyaev and T.G. Langdon: *Prog. Mater Sci.*, 2008, vol. 53, pp. 893–979.
24. M.J. Starink, X.C. Cheng, and S. Yang: *Acta Mater.*, 2013, vol. 61, pp. 183–92.
25. E.Y. Yoon, D.J. Lee, T.S. Kim, H.J. Chae, P. Jenei, J. Gubicza, T. Ungar, M. Janecek, J. Vratna, S. Lee, and H.S. Kim: *J. Mater. Sci.*, 2012, vol. 47, pp. 7117–23.
26. S. Lee, K. Edalati, and Z. Horita: *Mater. Trans.*, 2010, vol. 51, pp. 1072–79.
27. B. Joni, E. Schafler, M. Zehetbauer, G. Tichy, and T. Ungar: *Acta Mater.*, 2014, vol. 61, pp. 632–42.
28. Q. Wei, H.T. Zhang, B.E. Schuster, K.T. Ramesh, R.Z. Valiev, L.J. Kecskes, R.J. Dowding, L. Magness, and K. Cho: *Acta Mater.*, 2006, vol. 54, pp. 4079–89.
29. Y. Ikoma, K. Hayano, K. Edalati, K. Saito, Q. Guo, and Z. Horita: *Appl. Phys. Lett.*, 2012, vol. 101, p. 121908.
30. K. Edalati, S. Toh, Y. Ikoma, and Z. Horita: *Scripta Mater.*, 2011, vol. 65, pp. 974–77.
31. P.V. Liddicoat, X.Z. Liao, Y.H. Zhao, Y.T. Zhu, M.Y. Murashkin, E.J. Lavernia, R.Z. Valiev, and S.P. Ringer: *Nat. Commun.*, 2010, vol. 1, p. 63.
32. Y.H. Zhao, X.Z. Liao, S. Cheng, E. Ma, and Y.T. Zhu: *Adv. Mater.*, 2006, vol. 18, pp. 2280–83.
33. Z. Horita, K. Ohashi, T. Fujita, K. Kaneko, and T.G. Langdon: *Adv. Mater.*, 2005, vol. 17, pp. 1599–1602.
34. W.J. Kim, J.K. Kim, T.Y. Park, S.I. Hong, D.I. Kim, Y.S. Kim, and J.D. Lee: *Metall. Mater. Trans. A*, 2002, vol. 33, pp. 3155–64.
35. S. Takaki, K. Kawasaki, Y. Futamura, and T. Tsuchiyama: *Mater. Sci. Forum*, 2006, vols. 503–504, pp. 317–22.
36. K. Edalati and Z. Horita: *Acta Mater.*, 2011, vol. 59, pp. 6831–36.
37. K. Edalati, D. Akama, A. Nishio, S. Lee, Y. Yonenaga, J.M. Cubero-sesin, and Z. Horita: *Acta Mater.*, 2014, vol. 69, pp. 68–77.
38. J. Gubicza, N.Q. Chinh, J.L. Labar, S. Dobatkin, Z. Hegedus, and T.G. Langdon: *J. Alloys Compd.*, 2009, vol. 483, pp. 271–74.
39. B. Cao, S.P. Joshi, and K.T. Ramesh: *Scripta Mater.*, 2009, vol. 60, pp. 619–22.
40. H. Wen, T.D. Topping, D. Isheim, D.N. Fman, and E.J. Lavernia: *Acta Mater.*, 2013, vol. 61, pp. 2769–82.
41. J.S. Wang, M.D. Mulholland, G.B. Olson, and D.N. Seidman: *Acta Mater.*, 2013, vol. 61, pp. 4939–52.
42. K. Edalati, Z. Horita, and T.G. Langdon: *Scripta Mater.*, 2009, vol. 60, pp. 9–12.
43. G.K. Williamson and W.H. Hall: *Acta Mater.*, 1953, vol. 1, pp. 22–31.
44. K. Edalati, T. Fujioka, and Z. Horita: *Mater. Trans.*, 2009, vol. 50, pp. 44–50.
45. R.Z. Valiev, Y.V. Ivanisenko, E.F. Rauch, and B. Baudelet: *Acta Mater.*, 1996, vol. 44, pp. 4705–12.
46. A. Vorhauer and R. Pippan: *Scripta Mater.*, 2004, vol. 51, pp. 921–25.
47. M.T. Perez-Prado, A.A. Gimazov, O.A. Ruano, M.E. Kassner, and A.P. Zhilyaev: *Scripta Mater.*, 2008, vol. 58, pp. 219–22.
48. N.Q. Chinh, R.Z. Valiev, X. Sauvage, G. Varga, K. Havancsak, M. Kawasaki, B.B. Straumal, and T.G. Langdon: *Adv. Eng. Mater.*, 2014, vol. 16, pp. 1000–09.
49. Y. Harai, K. Edalati, Z. Horita, and T.G. Langdon: *Acta Mater.*, 2009, vol. 57, pp. 1147–53.
50. K. Edalati, T. Fujioka, and Z. Horita: *Mater. Sci. Eng. A*, 2008, vol. 497, pp. 168–73.
51. Y. Ito and Z. Horita: *Mater. Sci. Eng. A*, 2009, vol. 503, pp. 32–36.
52. M. Kawasaki, B. Ahn, and T.G. Langdon: *J. Mater. Sci.*, 2010, vol. 45, pp. 4583–93.
53. M. Kawasaki, R.B. Figueiredo, and T.G. Langdon: *Acta Mater.*, 2011, vol. 59, pp. 308–16.
54. A. Loucif, R.B. Figueiredo, T. Baudin, F. Brisset, R. Chemam, and T.G. Langdon: *Mater. Sci. Eng., A*, 2012, vol. 532, pp. 139–45.
55. M.R. Rezaei, M.R. Toroghinejad, and F. Ashrafizadeh: *J. Mater. Proc. Tech.*, 2011, vol. 211, pp. 1184–90.
56. T. Masuda, S. Hirosawa, Z. Horita, and K. Matsuda: *J. Jpn. Inst. Metals*, 2011, vol. 75, pp. 283–90.
57. S. Hirosawa, T. Hamaoka, Z. Horita, S. Lee, K. Matsuda, and D. Terada: *Metall. Mater. Trans. A*, 2013, vol. 44A, pp. 3921–33.
58. S. Mazzini and J.C. Caretti: *Scripta Metall. Mater.*, 1991, vol. 25, pp. 1987–90.
59. Z. Horita, T. Fujinami, M. Nemoto, and T.G. Langdon: *Metall. Mater. Trans. A*, 2000, vol. 31A, pp. 691–701.
60. I.F. Mohamed: Ph.D. Thesis, Kyushu University, 2015.
61. I.F. Mohamed, Y. Yonenaga, S. Lee, K. Edalati, and Z. Horita: *Mater. Sci. Eng., A*, 2015, vol. 627, pp. 111–18.
62. K. Edalati, J.M. Cubero-Sesin, A. Alhamidi, I.F. Mohamed, and Z. Horita: *Mater. Sci. Eng., A*, 2014, vol. 613, pp. 103–10.
63. U.F. Kocks, A.S. Argon, and M.F. Ashby: *Prog. Mater Sci.*, 1975, vol. 19, pp. 1–288.
64. R.L. Fleischer: *Acta Metall.*, 1963, vol. 11, pp. 203–09.
65. R. Labusch: *Acta Metall.*, 1972, vol. 20, pp. 917–27.
66. L. Vitos and B. Johanson: *Lect. Notes Comp. Sci.*, 2007, vol. 4699, pp. 510–19.
67. J.E. Bailey and P.B. Hirsch: *Philos. Mag.*, 1960, vol. 5, pp. 485–97.
68. A. Kelly and R. Nicholson: *Prog. Mater. Sci.*, 1963, vol. 10, pp. 151–391.
69. L.E. Murr: *Interfacial Phenomena in Metals and Alloys*, Addison-Wesley Publishing Company, Reading, MA, 1975.
70. E. Orowan: *Symposium on Internal Stresses in Metals and Alloys*, Institute of Metal, London, 1947, pp. 451–53.
71. D. Akama, S. Lee, Z. Horita, K. Matsuda, and S. Hirosawa: *Mater. Trans.*, 2014, vol. 55, pp. 640–45.